Conference on Modelling Fluid Flow (CMFF'25)
The 19th International Conference on Fluid Flow Technologies
Budapest, Hungary, August 26-August 29, 2025

MODULATING VORTEX DYNAMICS AROUND CIRCULAR CYLINDER VIA ASYMMETRIC CROSS-SECTIONAL PROFILE MORPHING: A COMPARATIVE STUDY OF CYLINDRICAL AND ELLIPTICAL CONFIGURATIONS

Kamila FETHALLAH[1], Mahmoud MEKADEM[1], Hamid OUALI[1]

[1] Fluid Mechanics Laboratory, Department of Fluid Mechanics and Energy,Ecole Militaire Polytechnique, PB N 17 Bordj El Bahri, Algiers, Algeria. *E-mail: fethallahcamela2@gmail.com

ABSTRACT

This research addresses the critical challenge of finding effective solutions to reduce drag and improve flow control around circular cylinders, which is essential for enhancing the performance and efficiency of various engineering systems. It presents an asymmetric flow control method utilising a crank mechanism to morph the cross-section from circular to elliptical via trailing edge motion. The study examines deformation amplitudes ranging from 10% to 20% and frequencies from 0.97 to 1.09, revealing that a 15% deformation amplitude at a near-natural shedding frequency ($f_d/f_0 = 1.07$) achieves a 44% drag reduction, attributed to reduced velocity deficits and suppressed turbulence intensity. Complementary numerical simulations employing RANS with the Spalart-Allmaras turbulence model at Re = 5600 broaden the analysis to extreme amplitudes (5%–100%) and frequencies ($f_d/f_0 = 0.1$–2.5), indicating that extreme amplitudes (100%) combined with low frequencies ($f_d/f_0 = 0.1$) yield a 42% drag reduction due to reduced recirculation zones. These findings highlight a critical nonlinear dependence of drag reduction on deformation parameters, suggesting asymmetric morphing as an effective strategy for enhancing aerodynamic efficiency in engineering applications.

Keywords: Control frequencies, deformation amplitudes, drag coefficient, elliptical cylindrical deformation, flow dynamics, wake pattern.

1. INTRODUCTION

Active flow control (AFC) dynamically alters fluid behavior with the usage of external energy, solving issues such as drag reduction and boundary layer separation [1, 2]. In contrast to passive control approaches, AFC uses strategies like moving surfaces and synthetic methods to enhance efficiency in aerodynamic and hydrodynamic systems [3]. Boundary layer suppression is a primary goal, which is particularly important for streamlined flow in offshore constructions, turbines, and airfoils [4].

The flow around circular cylinders, a canonical fluid dynamics problem, reveals phenomena like vortex shedding and turbulence transition [5]. Omnipresent in engineering systems like heat exchangers and offshore risers, cylinders require advanced flow control to mitigate drag and vibrations [6], while their environmental impact on sediment transport necessitates optimized designs [7]. Among AFC techniques, movable walls have emerged as a transformative approach, directly modifying near-wall dynamics to delay separation and suppress vortices. These methods energize the boundary layer via surface motion such as rotating cylinders or virtual actuation via dielectric barrier discharge plasma actuators, achieving drag reductions of up to 25% [8, 9].

The effectiveness of movable walls relies on boundary layer manipulation such as high momentum fluid injection to impede adverse pressure gradients [8] to suppress vortex shedding, which is broken up into Von Kármán vortices to damp unsteady forces [4, 9]. Actuation techniques range from active compliant walls with embedded sensors [9], virtual surfaces using plasma actuators [8], to rotating cylinders [10], all validated through numerical and experimental tools. Laminar and Discrete Vortex Methods and Lattice Boltzmann Methods are employed to model hybrid passive-active control [11], while finite element models are used to simulate fluid-structure interaction [12]. Experimentally, wind tunnel tests, particle image velocimetry, and force measurements quantify performance, linking pressure distributions to aerodynamic loads [13, 14].

A modern trend in development integrates machine learning (ML) with active flow control setups, where deep reinforcement learning (DRL) provides

real-time actuation strategies by learning from CFD data [3, 15]. Data-driven approaches propose genetic programming for control-law synthesis [16] and neural ordinary differential equations for fast predictions [17], filling gaps between model- and data-based frameworks. Such ML-based strategies have a profound impact on next-generation flow control systems by enhancing adaptability and computational efficiency.

Building on this interplay between control and fluid dynamics, this paper introduces asymmetric morphing for circular cylinder flow control by means of the periodic motion of the cylinder's trailing edge, as contrasted with traditional methods via radial deformation symmetric with respect to the cylinder axis of oscillation [18, 19, 20] or rotational oscillation of the whole cylinder [21]. Unlike classical momentum injection techniques such as plasma actuators [8] or rotating surfaces [10], the proposed method induces a dynamic transition of the cylinder's cross-section between circular and elliptical configurations using a crank system. The resulting asymmetric, time-varying curvature serves to halt boundary layer separation and vortex coherence.

To quantify the impact of this control technique on flow dynamics, tests were conducted experimentally at Re = 8800, for nine deformation frequencies and three amplitudes, whereas numerical simulations were performed at Re = 5600, for seven frequencies and amplitudes from 5% to 100%. The study endeavors, therefore, through this combined assessment, to work out how the deformation parameters interact with intrinsic flow instabilities in regard to issues where drag proves critical.

NOMENCLATURE

D	[m]	diameter
$\Delta d/d$	[-]	deformation amplitude
f_d	[Hz]	deformation frequency
f_0	[Hz]	natural emission frequency
f_{sh}	[Hz]	vortex emission frequency
R_e	[-]	Reynolds number
S_t	[-]	Strouhal number
U_∞	[m/s]	free flow velocity
U_{mean}	[m/s]	mean speed
U_{RMS}	[m/s]	root mean square speed
C_d	[-]	drag coefficient
C_{d0}	[-]	nominal drag coefficient
C_l	[-]	lift coefficient
R	[-]	drag coefficient reduction rate
T	[N]	drag force
H	[m]	vertical length of measurement
l	[m]	cylinder length
ρ	[kg/m^3]	flow density
$u(t)$	[m/s]	instantaneous velocity signal
$u'(t)$	[m/s]	turbulent velocity fluctuations
x, y	[m]	axial, transversal (coordinate)

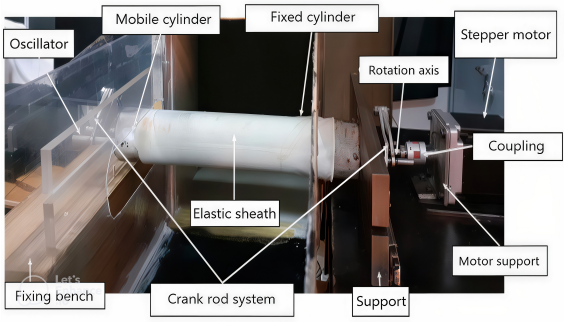

Figure 1. Assembly of mock-up.

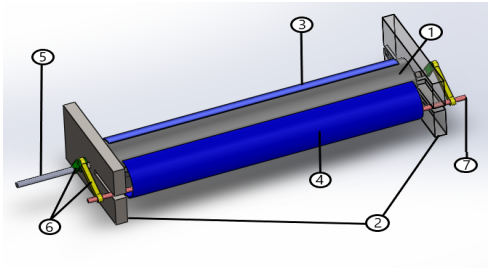

Figure 2. Isometric view of the mock-up.

2. EXPERIMENTAL APPARATUS AND PROCEDURE

2.1. EXPERIMENTAL SETUP

Experiments are performed using the setup illustrated in Fig. 1, which consists of an open-type subsonic wind tunnel (Eiffel HM 170), a hot-wire anemometer, a stepping motor, and a power supply. The wind tunnel features a test section of 292×292 mm^2, a maximum air velocity of 28 m/s, and a turbulence intensity of 1%, allowing for precise flow measurements.

An isometric view of the morphing cylinder assembly is shown in Fig. 2. The model consists of a steel tube (1) flush-mounted to support structures (2) and divided into two aluminum halves: one fixed (3) and the other movable (4), enabling the transition between circular and elliptical cross-sections. The transverse diameter remains constant, while the longitudinal diameter varies through controlled deformation. The assembly is enclosed by an elastic sheath to preserve aerodynamic integrity and maintain consistent surface contact. A stepper motor drives the system via a crank mechanism (6) and an oscillator (7), translating rotary motion into sinusoidal linear displacement of the movable wall. The deformation amplitude and frequency are controlled using an Arduino board, ensuring synchronized actuation without edge misalignment.

2.2. Calibration and procedure

The hot-wire anemometer is calibrated using the Dantec Dynamics StreamLine® Pro Automatic Calibrator, ensuring high precision for velocity calibration within the expected range, not exceeding 5 m/s.

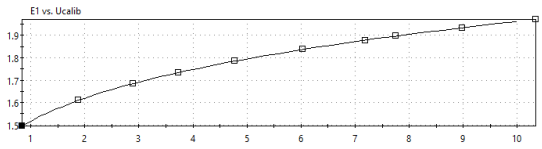

Figure 3. Calibration of the hot-wire sensor.

According to the manufacturer's user manual, the velocity uncertainty at the nozzle outlet during proper calibration is specified as ±1% ±0.02 m/s. The calibration process generates a dataset comprising corrected voltage readings (accounting for temperature fluctuations) and a third-order calibration polynomial. These outputs are illustrated in Fig. 3.

The cylinder is positioned perpendicular to the flow, the hot-wire anemometer taking measurements at a point $3.5D$ downstream from the cylinder's trailing edge ($D = 0.063$ m) and at 0.05 m from the plates. The velocity of the incident flow is 2.5m/s, which corresponds to a Reynolds number based on the initial diameter $Re = 8.8 \times 10^3$. The specific measurement distance was arrived at through an iterative adjustment process intended to properly compensate for inherent physical flow behavior involved in vortex shedding under the natural, uncontrolled condition.

3. NUMERICAL METHOD

The finite-volume method is used to discretize the governing equations, which is employed to perform RANS simulation. The geometric model setup and mesh generation is carried out by GAMBIT, which is the preprocessor of FLUENT.

3.1. Computational setup

The accuracy of computations in fluid dynamics is influenced by grid and computational domain dimensions, particularly when using dynamic meshing to evaluate aerodynamic coefficients. The computational domain [20] (Fig.4) spans $8D$ upstream and $20D$ downstream of the cylinder, with lateral surfaces at $8D$ above/below. For 3D simulations, the domain is extruded along the span (length πD), with $8D$ upstream for flow development and $20D$ downstream for wake analysis. The domain is subdivided into four zones (Fig. 5): Zone 1 (adjacent to the cylinder) uses a refined structured mesh (first grid point at $y^+ = 1$) and is mobile via a User Defined Function (UDF) to model the cylinder's moving wall. This zone undergoes translational motion while maintaining a non-deformable mesh. Zones 2-3 are structured, and Zone 4 is coarsely meshed due to weak physical gradients. Non-conforming interfaces preserve flow accuracy between zones, ensuring fidelity to the experimental geometry.

Table 1. Solver validation.

Author	Re	Method	C_d
Lourenco et Shih [22]	3900	Exp	0.98
Kahil [23]	4020	LES	1.02
Young et Ooi [24]	3900	RANS 2D	1.59
Present work	3470	K-Wsst	0.918
Present work	3470	Spalart-Allmaras	0.974
Present work	3470	K-ω	0.81

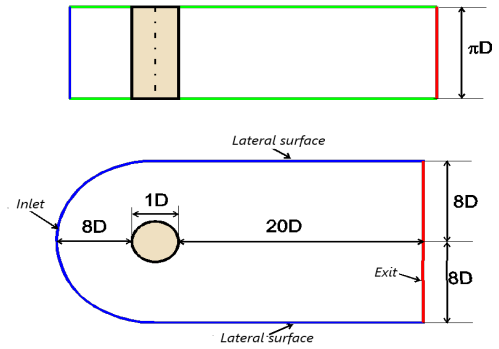

Figure 4. Calculation range and boundary conditions.

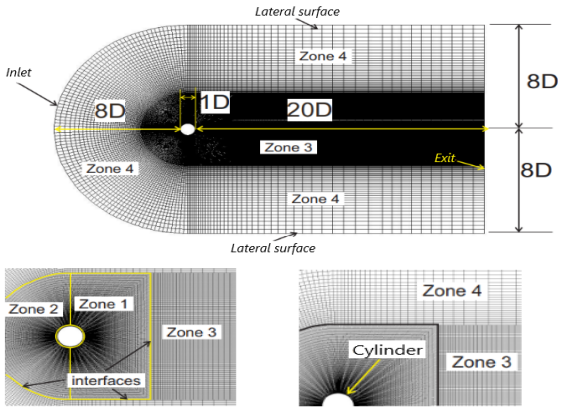

Figure 5. Calculation domain and mesh strategy adopted.

3.2. Solver validation

The drag (C_d) coefficient obtained with different models (Spalart-Allmaras, K-ω SST and K-ω) is compared with those of the experimental work of Lourenco and Shih [22], as reported in Table 1. The results show that the Spalart-Allmaras model gives a good estimate of C_d, with a relative error of 1% compared with the experimental work, while the K-ω SST and K-ω models present relative errors of 6% and 17% respectively, according to the data in Table 1, which leads to the adoption of the Spalart-Allmaras model for simulations with a moving downstream wall.

4. RESULTS AND DISCUSSION

4.1. Experimental results

Instantaneous velocity measurements $u(t)$, obtained by hot-wire anemometry, are used to characterize the vortex dynamics and wake generated by

Table 2. Cases treated with hot wire.

Deformation rate	f_d	f_d/f_0
$\Delta d/d = 0.10$	data1 : 6.60	0.97
	data2 : 6.70	0.98
	data3 : 6.80	1.00
$\Delta d/d = 0.15$	data4 : 6.90	1.01
	data5 : 7.00	1.03
	data6 : 7.10	1.04
$\Delta d/d = 0.20$	data7 : 7.20	1.06
	data8 : 7.30	1.07
	data9 : 7.40	1.09

the cylinder. The $u(t)$ signal is decomposed into a mean component U_{mean} and turbulent fluctuations $u'(t)$, such that:

$$u(t) = U_{\text{mean}} + u'(t), \tag{1}$$

$$\text{with} \quad U_{\text{mean}} = \frac{1}{T}\int_0^T u(t)\,dt, \tag{2}$$

$$\text{and} \quad U_{\text{RMS}} = \sqrt{\frac{1}{T}\int_0^T (u'(t))^2\,dt}. \tag{3}$$

The Fourier transform (FFT) of $u'(t)$ reveals the natural vortex shedding frequency, denoted f_0. The mean velocity U_{mean} not only allows the evaluation of the velocity deficit, which is related to drag, but also enables the indirect estimation of the drag coefficient C_d. The RMS level of $u(t)$, U_{RMS}, reflects the wake thickness and is associated with turbulence intensity. These results show how the elliptical deformation influences these various parameters.

The cases studied experimentally using hot-wire measurements are presented in Table 2.

4.1.1 *Vortex-shedding frequency*

To study the flow around a cylinder, it is crucial to determine the natural emission frequency of the vortices. The Fourier transform of the instantaneous velocity signal recorded at $x/d = 3.5$, downstream of the vortex formation zone, was used to analyse the frequency content of the fluctuating signal. The frequency detected, $f_0 = 3.401$ Hz (Fig.6), led to a natural emission frequency equivalent to twice this value.

The corresponding Strouhal number, $S_t = 0.21$, calculated using the formula $S_t = 2f_0 d/U_\infty$, aligns perfectly with the Reynolds number considered ($Re = 8800$), in agreement with the results of Norberg et al. [25].

For controlled cases, modulation of the wake frequency by the deformation frequencies imposed on the cylinder was observed. For $\Delta d/d = 10\%$, the vortex emission frequency spectra (Fig.7) show a broad band of peaks around the natural frequency, with a transition to wake synchronization for deformation frequencies around $f_d/f_0 = 1.04$, indicating a complex interaction between cylinder deformation and wake dynamics.

For $\Delta d/d = 15\%$, the variation in deformation frequencies caused the main peaks in the vortex emission frequency spectra to fluctuate around

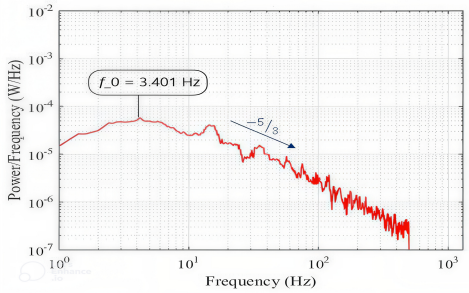

Figure 6. Spectrum of velocity fluctuations at $x/d = 3.5$ on the wake centreline.

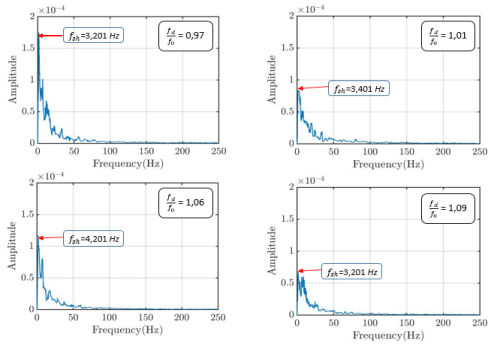

Figure 7. Vortex emission frequency at a point located at x/d 3.5 on the wake centreline for a central line of the wake for a deformation of 10%.

the natural frequency range (Fig.8). The modulation of the vortex emission frequency by the deformation frequencies coincided for $f_d/f_0 = 0.97$. Increasing the deformation frequency caused the peak emission frequency to exceed that of the natural case, likely due to the interaction between the deformation of the cylinder's moving wall and the vibration of the mechanism.

For $\Delta d/d = 20\%$, the emission frequency was practically identical to the natural frequency for $f_d/f_0 = 0.79$. The increase in deformation frequencies led to a considerable amplification of the spectral peak (Fig.9), with an emission frequency exceeding that of the natural case. This is explained by reson-

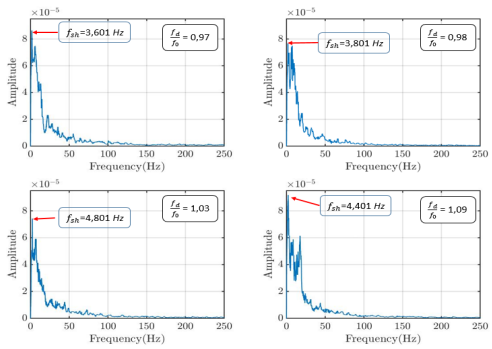

Figure 8. Vortex emission frequency at a point located at x/d 3.5 on the wake centreline for a central line of the wake for a deformation of 15%.

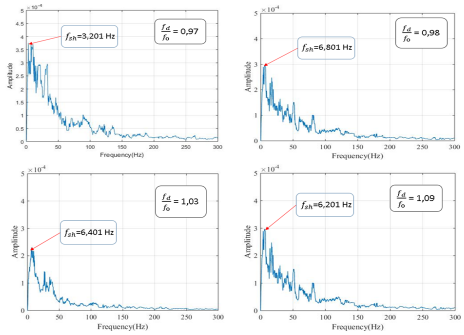

Figure 9. Vortex emission frequency at a point located at x/d 3.5 on the wake centreline for a central line of the wake for a deformation of 20%**.**

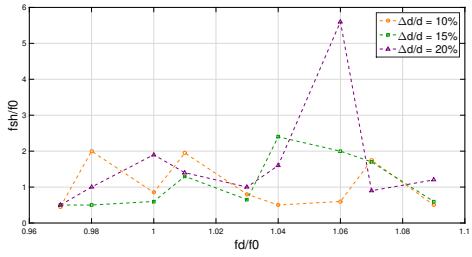

Figure 10. Effect of deformation frequency on vortex emission frequency.

ance when the flow is controlled with a frequency close to its natural frequency, suggesting that cylinder deformation can control and modify wake dynamics.

The effect of the control frequency on the vortex emission frequency varies with deformation amplitude (Fig.10). At 10%, the vortex emission frequency fluctuates around twice the deformation frequency, with a minimum at $f_{\text{sh}}/f_0 = 0.76$. At 15%, it varies around the cylinder's deformation frequency, with extrema at $f_{\text{sh}}/f_0 = 0.5$ and $f_{\text{sh}}/f_0 = 2.4$. At 20%, the vortex emission frequency exceeds five times the deformation frequency, peaking at $f_{\text{sh}}/f_0 = 5.80$ for $f_d/f_0 = 1.06$, showing the influence of deformation amplitude on vortex emission frequency.

4.1.2 Transverse mean velocity

Figures 11, 12, and 13 show the mean transverse velocity profiles normalized by the incident flow velocity, measured at $x/d = 3.5$ from the centre of the cylinder, for different deformation amplitudes ($\Delta d/d = 10\%$, 15%, and 20%) and deformation frequencies.

At 10% amplitude (Fig. 11), the mean velocity remains higher than the nominal case at all frequencies, with a reduction in the velocity deficit associated with a downward deflection of the wake, suggesting a reduction in drag.

At 15% (Fig. 12), the decrease in velocity deficit becomes more pronounced, confirming a more significant reduction in drag while retaining the favorable wake deflection.

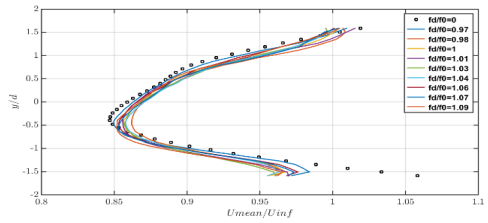

Figure 11. Wake deficit at $x/d = 3.5$ for various strain frequencies at 10% **amplitude.**

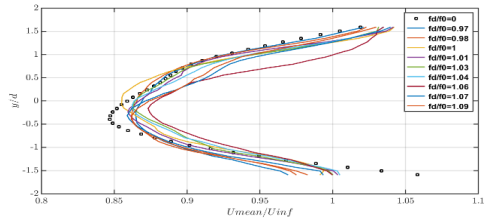

Figure 12. Wake deficit at $x/d = 3.5$ for various strain frequencies at 15% **amplitude.**

However, at 20% (Fig. 13), the behaviour becomes mixed: certain frequencies (0.97, 0.98, 1.00, 1.04) amplify the speed and reduce the deficit, while others (1.01, 1.03, 1.06, 1.07, 1.09) degrade these parameters, increasing the speed deficit.

The optimal state is identified at 15% amplitude with a frequency $fd/f_0 = 1.07$, offering the maximum reduction in velocity deficit and maintaining downward wake deflection, making it the most favourable scenario for drag control.

4.1.3 Root mean square of the transverse velocity fluctuations

The analysis of the distributions of the relative standard deviation (U_{RMS}/U_∞) for different strain amplitudes ($\Delta d/d$) and strain frequencies (f_d/f_0) highlights specific behaviours. For $\Delta d/d = 10\%$ (Fig. 14), the distance between the two peaks is greater than that of the nominal case for all frequencies. For $\Delta d/d = 15\%$ (Fig. 15), the distance between the peaks varies with frequency, increasing for low frequencies and notably decreasing for higher frequencies, resulting in a reduction of the wake thickness and a delay in separation. Finally, for $\Delta d/d = 20\%$ (Fig. 16), the distance between the peaks is minimal for all frequencies, with a near dis-

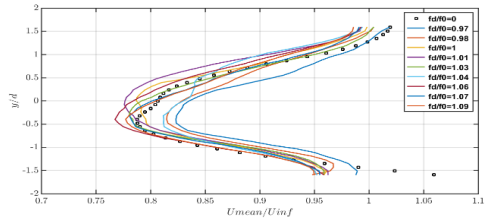

Figure 13. Wake deficit at $x/d = 3.5$ for various strain frequencies at 20% **amplitude.**

appearance of the peaks for $f_d/f_0 = 1.04$, indicating a reduction in the wake thickness and a delayed separation, which suggests that this deformation amplitude is the most favourable for reducing drag.

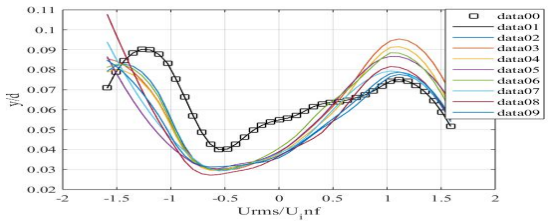

Figure 14. Root-mean-square of velocity fluctuations at $x/d = 3.5$ for a 10% deformation.

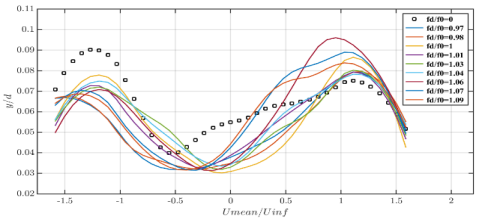

Figure 15. Root-mean-square of velocity fluctuations at $x/d = 3.5$ for a 15% deformation.

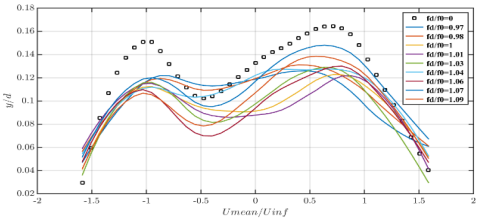

Figure 16. Root-mean-square of velocity fluctuations at $x/d = 3.5$ for a 20% deformation.

4.1.4 Drag coefficient

The drag coefficient is defined as the ratio between the drag force and the dynamic energy of the flow. It is calculated by integrating the velocity profile u/U as a function of y/D, from the drag force equation:

$$T = \int_{-H}^{H} \rho l u (U_\infty - u)\,\mathrm{d}y \tag{4}$$

Where T is the drag force, H is the vertical length of measurement, l is the cylinder length, u is the mean velocity, U_∞ is the incident flow velocity, and ρ is the flow density.
The drag coefficient is defined by:

$$C_d = \frac{T}{\frac{1}{2}\rho U_\infty^2 D l} \Rightarrow C_d = 2\int_{-H}^{H} \frac{u}{U_\infty}\left(1 - \frac{u}{U_\infty}\right)\mathrm{d}\left(\frac{y}{D}\right) \tag{5}$$

This method allows the drag to be evaluated from velocity measurements.

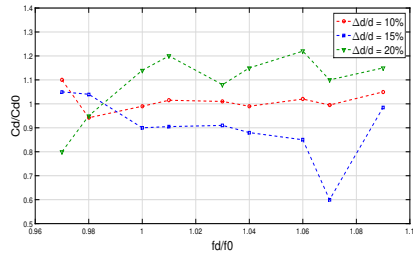

Figure 17. Variation in drag coefficient as a function of control frequency.

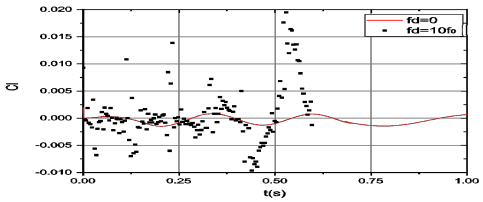

Figure 18. Instantaneous variation in lift coefficient.

Figure 17 highlights how the drag coefficient (C_d) varies as a function of control frequency (f_d/f_0) for different strain amplitudes ($\Delta d/d$). For a strain amplitude of 10%, the reduction in C_d is small (6%) and remains close to the nominal value. On the other hand, for $\Delta d/d = 15\%$, there is a significant reduction in C_d (44%) at $f_d/f_0 = 1.07$, while for $\Delta d/d = 20\%$, the greatest reduction in drag occurs at $f_d/f_0 = 0.97$, with a reduction of 21%. These results indicate that strain amplitude and control frequency strongly influence drag, with greater reductions for higher strain amplitudes and specific control frequencies.

4.2. Numerical results

Given the negligible mean lift coefficient ($C_l \approx 0$) and its minor fluctuations around this value during vortex shedding (Fig.18) consistent with prior findings by Rezaiguia and Ghouali [21] this analysis focuses exclusively on the drag coefficient (C_d). Specifically, the influence of deformation amplitudes ($\Delta d/d$) and frequencies (f_d/f_0) in Table 3 on the mean drag coefficient (C_d) and its root-mean-square (RMS) fluctuations is evaluated. These parameters are detailed in the following sections.

4.2.1 Drag coefficient reduction rate

The results were analyzed in order to obtain average values of drag coefficients and drag gains: $R = (\frac{C_d - C_{d0}}{C_{d0}}) * 100$, by varying the frequency and amplitude of the deformation of the cylinder cross-section. The obtained results show that in all the

Table 3. Cases treated numerically.

f_d/f_0		0.1	0.25	0.5	1.0	1.5	2.0	2.5	
$\Delta d/d$%	5	10	20	30	40	50	60	80	100

Table 4. Drag reduction rates obtained for different frequencies and amplitudes.

$\Delta d/d\%$ \ f_d/f_0	0,1	0,25	0,5	1,0	1,5	2,0	2,5
5	-18,87	-22,18	-23,44	-23,80	-23,51	-23,07	-22,59
10	-20,35	-23,61	-24,21	-24,51	-23,86	-22,39	-22,27
20	-23,42	-25,84	-26,00	-25,83	-24,27	-22,06	-19,90
30	-26,93	-28,46	-28,41	-27,56	-24,84	-21,08	-21,18
40	-30,42	-31,62	-31,29	-29,36	-26,11	-20,55	-20,35
50	-33,29	-34,44	-33,49	-31,34	-27,62	-20,55	-20,45
60	-18,87	-36,50	-35,08	-33,21	-28,33	-20,09	-20,23
80	-39,49	-39,54	-37,23	-37,29	-26,65	-17,54	-16,36
100	-41,92	-41,65	-38,80	-37,40	-23,65	–	-5,391

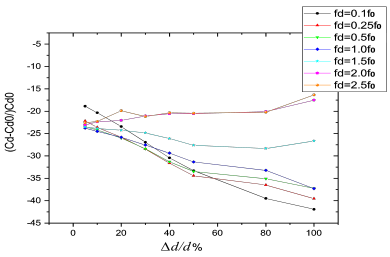

Figure 19. Drag reduction rates as a function of frequency and amplitude.

considered cases, drag reduction rates are negative, hence proving that a reduction in drag has been obtained. These results are summarized in Table 4.

The results obtained in the table are represented graphically in Fig. 19, where it can be noticed that the best reductions (R_{max} = 42%) are obtained for the lowest frequency (f_d/f_0 = 0.1) combined with the highest amplitudes ($\Delta d/d$ = 100%). The minimum drag reduction rates (R_{min} = 5.4%) are obtained with the highest frequencies combined with the highest amplitudes. Thus, the most favourable drag reductions are obtained for the smallest frequencies.

4.2.2 Root Mean Square (RMS) of drag coefficient

Figure 20 shows the evolution of the RMS as a function of the amplitude and frequency of deformation of the cylinder. It shows that the intensity of the turbulence increases proportionally to the frequency and amplitude. As mentioned earlier, this increase is synonymous with an increase in the turbulent kinetic energy in the flow and the energy transported by the vortex structures emitted by the cylinder.

As previously stated, this increase is synonymous with an increase in the turbulent kinetic energy of the flow and the energy transported by the vortex structures emitted by the cylinder. On the other hand, a reduction in turbulent kinetic energy leads to a more stable flow around bluff bodies, which reduces the variability of the drag coefficient, as indicated by a lower RMS.

5. CONCLUSION

This study explores the effectiveness of cylindrical-elliptical deformation of a circular cylinder's cross-section for active flow control, conducted in a subsonic wind tunnel at a Reynolds number of Re = 8800. The experimental results

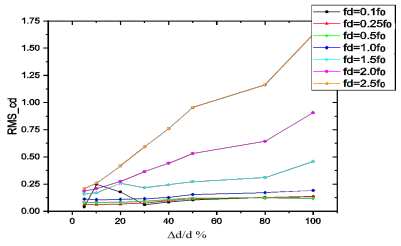

Figure 20. Root-mean-square of fluctuations in drag coefficient.

indicate that deformation significantly influences vortex dynamics, with a maximum drag coefficient reduction of 44% observed at a 15% deformation amplitude and a frequency ratio of f_d/f_0 = 1.07. At a 10% amplitude, the drag reduction is modest at 6%, while at 20% amplitude, a maximum reduction of 21% is achieved at f_d/f_0 = 0.97.

Numerical simulations using the RANS approach with the Spalart-Allmaras model confirm these findings, showing a drag reduction of up to 42% at a 100% deformation amplitude and a low frequency of f_d/f_0 = 0.1. The analysis reveals that lower frequencies and higher amplitudes lead to enhanced flow stability and reduced recirculation zones.

Additionally, the study highlights that the root mean square (RMS) of velocity fluctuations decreases with increased deformation amplitude, indicating reduced wake thickness and delayed flow separation. The modulation of vortex shedding frequency by deformation frequencies demonstrates synchronization effects, particularly at f_d/f_0 ratios near 1, which are crucial for optimizing drag reduction.

REFERENCES

[1] Vakhshouri, M. E., and Çuhadaroğlu, B., 2022, "Effects of uniform injection and suction through perforated pentagonal cylinders on the flow and heat transfer", *International Journal of Numerical Methods for Heat & Fluid Flow*, Vol. 32 (4), pp. 1324–1347.

[2] Ahmad, M., Qayoum, A., Dilawar, M., Bhat, G. S., and Sofi, A. Y., 2025, "Experimental investigation of the effects of cavity design for flow characteristics and heat transfer properties of synthetic jet actuators in quiescent flow", *Journal of Thermal Analysis and Calorimetry*, pp. 1–18.

[3] Jiang-Li, C., Shao-Qiang, C., Feng, R., and Hai-Bao, H., 2022, "Artificially intelligent control of drag reduction around acircular cylinder based on wall pressure feedback br", *ACTA PHYSICA SINICA*, Vol. 71 (8).

[4] Koc, I., 2008, *Experimental investigation of active control of bluff body vortex shedding*, Old Dominion University.

[5] Sarwar, W., 2020, "Active flow control methods for aerodynamic applications", .

[6] Zhao, M., 2023, "A review of recent studies on the control of vortex-induced vibration of circular cylinders", *Ocean Engineering*, Vol. 285, p. 115389.

[7] Choi, S.-D., Eum, T.-S., Shin, E. T., and Song, C. G., 2021, "Numerical investigation of flow around a structure using Navier-slip boundary conditions", *World Journal of Engineering*, Vol. 19 (5), pp. 667–674.

[8] Zhang, X., Choi, K.-S., Huang, Y., and Li, H.-x., 2019, "Flow control over a circular cylinder using virtual moving surface boundary layer control", *Experiments in fluids*, Vol. 60, pp. 1–15.

[9] Pal, D., Sinha, S., Pal, D., and Sinha, S., 1997, "Controlling an unsteady separating boundary layer on a cylinder with an active compliant wall", *35th Aerospace Sciences Meeting and Exhibit*, p. 212.

[10] Bergmann, M., Cordier, L., and Brancher, J.-P., 2005, "Optimal rotary control of the cylinder wake using proper orthogonal decomposition reduced-order model", *Physics of fluids*, Vol. 17 (9).

[11] Oliveira, M. A. d., Moraes, P. G. d., Andrade, C. L. d., Bimbato, A. M., and Alcântara Pereira, L. A., 2020, "Control and suppression of vortex shedding from a slightly rough circular cylinder by a discrete vortex method", *Energies*, Vol. 13 (17), p. 4481.

[12] Chua, M. H., and Liu, B., 2024, "Active Flow Control of Flow Over a Stationary Cylinder Using a Flapping Rod at Low Reynolds Number", *International Conference on Offshore Mechanics and Arctic Engineering*, American Society of Mechanical Engineers, Vol. 87844, p. V006T08A017.

[13] Akbıyık, H., and Akansu, Y., 2021, "Effective flow control around a circular cylinder by using both a splitter plate and plasma actuators as passive and active control methods", *Isı Bilimi ve Tekniği Dergisi*, Vol. 41 (1), pp. 133–140.

[14] Santhanakrishnan, A., Jacob, J., and Suzen, Y., 2006, "Flow control using plasma actuators and linear/annular plasma synthetic jet actuators", *3rd AIAA Flow Control Conference*, p. 3033.

[15] Ren, F., Rabault, J., and Tang, H., 2021, "Applying deep reinforcement learning to active flow control in weakly turbulent conditions", *Physics of Fluids*, Vol. 33 (3).

[16] Ren, F., Wang, C., and Tang, H., 2019, "Active control of vortex-induced vibration of a circular cylinder using machine learning", *Physics of Fluids*, Vol. 31 (9).

[17] Mao, Y., Zhong, S., and Yin, H., 2024, "Model-based deep reinforcement learning for active control of flow around a circular cylinder using action-informed episode-based neural ordinary differential equations", *Physics of Fluids*, Vol. 36 (8).

[18] Oualli, H., 2006, "Influence de la vibration radiale et de la rotation d'un cylindre circulaire sur l'évolution du sillage proche", Ph.D. thesis, Alger.

[19] Menfoukh, L., Hanchi, S., Oualli, H., Bouabdellah, A., and Askovic, R., 2008, "Experimental investigation of a circular radially deforming cylinder near wake using an infrared technique", *International journal of heat and fluid flow*, Vol. 29 (2), pp. 479–494.

[20] Aguedal, L., Semmar, D., Berrouk, A. S., Azzi, A., and Oualli, H., 2018, "3D vortex structure investigation using Large Eddy Simulation of flow around a rotary oscillating circular cylinder", *European Journal of Mechanics-B/Fluids*, Vol. 71, pp. 113–125.

[21] Rezaiguia, H., Ghoualli, M., and Oualli, H., 2021, "Experimental investigation of the flow behind a circular cylinder controlled by combination of a rotary oscillation and a radial deformation", *Journal of the Brazilian Society of Mechanical Sciences and Engineering*, Vol. 43 (5), p. 267.

[22] Lourenco, L., 1993, "Characteristics of the plane turbulent near wake of a circular cylinder", *A particle image velocimetry study*.

[23] Kahil, Y., 2011, "Simulation des grandes échelles d'écoulements turbulents autour de cylindres circulaires à un nombre de Reynolds sous critique", Ph.D. thesis, Paris 6.

[24] Young, M., and Ooi, A., 2007, "Comparative assessment of LES and URANS for flow over a cylinder at a Reynolds number of 3900", .

[25] Norberg, C., 1994, "An experimental investigation of the flow around a circular cylinder: influence of aspect ratio", *Journal of Fluid Mechanics*, Vol. 258, pp. 287–316.